

Ageing studies of Multi-Strip Multi-Gap Resistive Plate Counters based on low resistivity glass electrodes in high irradiation dose

D. Bartos^a, C. Burducea^c, I. Burducea^c, G. Caragheorgheopol^a, F. Constantin^c, L. Craciun^c, D. Dorobantu^a, M. Ghena^e, D. Iancu^c, A. Marcu^e, G. Mateescu^a, P. Mereuta^c, V. Moise^b, C. Negrila^d, D. Negut^b, M. Petris^a, M. Petrovici^a, L. Radulescu^a, V. Aprodu^a, L. Prodan^a, A. Radu^a and G. Stoian^a

^aHadron Physics Department, National Institute for Physics and Nuclear Engineering - IFIN-HH, P.O. Box MG-6, Bucharest-Magurele, Romania

^bMultipurpose Irradiation Centre, National Institute for Physics and Nuclear Engineering - IFIN-HH, P.O. Box MG-6, Bucharest-Magurele, Romania

^cApplied Nuclear Physics Department, National Institute for Physics and Nuclear Engineering - IFIN-HH, P.O. Box MG-6, Bucharest-Magurele, Romania

^dNational Institute of Materials Physics, INCDFM, P.O. Box MG-7, Bucharest-Magurele, Romania

^eInstitute for Laser, Plasma and Radiation Physics - INFLPR, P.O. Box MG-36, Bucharest-Magurele, Romania

ARTICLE INFO

Keywords:

Multi-Strip, Multi-Gap RPCs
high counting rate
ageing, high irradiation dose
SEM, XPS, foil-ERDA, RBS, AFM,
THz-TDS

ABSTRACT

Detailed tests and analysis of ageing effects of high irradiation dose on Multi-Strip Multi-Gap Resistive Plate Counters (MSMGRPC) based on low resistivity glass electrodes, foreseen to be used for the most forward polar angles covered by the Time-of Flight (ToF) sub-detector of the Compressed Baryonic Matter (CBM) experiment at Facility for Antiprotons and Ion Research (FAIR) - Darmstadt are reported. The tests were performed at a multi-purpose irradiation facility of IFIN-HH based on ⁶⁰Co source. MSMGRPC efficiency, cluster size, surface and volume resistivity of the glass electrodes after irradiation are measured and compared with their values before irradiation. The results of a comprehensive analysis of the composition and properties of the deposited layers on the glass electrodes, based on different methods, i.e. Scanning Electron Microscope (SEM), X-ray Photoelectron Spectroscopy (XPS), foil Elastic Recoil Detection Analysis (ERDA), Rutherford Backscattering Spectrometry (RBS), Atomic Force Microscopy (AFM) and Terahertz Time Domain Spectroscopy (THz-TDS), are presented.

1. Introduction

As it is well known, multi-differential analysis in hadron collisions at relativistic and ultra-relativistic energies, especially for rare probes, mandatory for understanding the underlying physics behind the observed phenomena, requires unprecedented high statistics. This could be achieved in a reasonable time using high luminosity or high intensity beams and performant experimental setups in high counting rate environment. One such example is the CBM experiment at FAIR-Darmstadt [1] which is foreseen to cope with interaction rates up to 10^7 events/sec for Au-Au collisions at $\sqrt{s_{NN}} = 2-5$ GeV which, due to kinematical focussing, produce charged particles counting rate of $\approx 3 \cdot 10^4$ (charged particles)/cm²·sec and ≈ 1 hit/cm² at the smallest polar angles covered by the experiment. One of the main component of the CBM experimental setup is the ToF sub-detector based on multi-gap resistive plate counters (MGRPC) [2].

*Corresponding author: M. Petrovici

ORCID(s): 0000-0002-7783-9029 (M. Petrovici)

Detailed R&D studies showed that Multi-Strip Multi-Gap Resistive Plate Counters (MSMGRPC) based on float glass could reach efficiency better than 95%, time resolution around 60 psec, position resolution across the strips of $\sigma_y \leq 1.7$ mm and along the strips of $\sigma_z \leq 1.55$ cm [3, 4, 5]. FOPI [6] was the first large experiment using a time-of-flight barrel based on MSMGRPC and among the first ones using MRPCs, HADES [7], STAR [8] and ALICE [9]. The R&D activity continued in order to develop MSMGRPCs which fulfil the above mentioned requirements for the CBM experimental setup in terms of high counting rate [10], high granularity [11], tunable transmission line impedance to be matched to the frontend electronics [12] with efficiency better than 95% and time resolution around 50 psec [13], based on low resistivity Pestov glass [10] or Chinese glass electrodes [14]. High counting rate test done at COSY-Julich using direct proton beam of 2.5 GeV/c showed a time resolution better than 70 ps and efficiency higher than 90% even at 10^5 protons/cm²·sec [11]. Test of the counter performance in high counting rate all over the counter area was done at SIS18-GSI-Darmstadt using charged particles produced by Ni beam of 1.7 A·GeV on 1mm thick Pb target up to the highest intensity per spill delivered by SIS18 [2]. No deterioration of the counter performance in terms of time resolution and efficiency was observed up to 10^4 particles/cm²·sec. As CBM experiment is foreseen to run 2 months/year for about 10 years, ageing tests in high irradiation dose are mandatory in order to guarantee that such a detector will maintain its performance over the whole lifetime of the experiment. Timing MRPCs reach very good time resolution and efficiency performance based on multi-gap structure and floating glass electrodes, flushed with C₂H₂F₄ + SF₆ + C₄H₁₀ gas mixture with different relative weights. Therefore, Si from the resistive glass electrodes, known as being highly volatile, with high probability to produce polymeric structure as well as the polymerisation of hydrocarbons from the gas mixture are the main components which contribute to the production of reactive species in polymerisation or chemical deposition in high density avalanches induced by high irradiation dose environment. Detailed studies of ageing phenomena, as the result of two competitive phenomena, i.e. ablation and polymerisation, in low pressure plasma were published in Ref. [15]. Long term ageing studies for timing MGRPC based on resistive electrodes, at a modest counting rate and total accumulated charge, and analysis of the deposited material on the electrodes were also published [16]. Ageing effects on the performance of the MSMGRPC based on low resistivity glass electrodes in very high irradiation dose and short time exposure, together with detailed analysis of the ablation/etching, deposited material and electric properties of the glass electrodes after the irradiation are reported in the present paper.

A short description of the detector architecture and test results before the irradiation are presented in Chapter 2. Irradiation experimental setup, its operation, control and measurement results during the irradiation are detailed in Chapter 3. In Chapter 4 are presented and discussed the tests after the irradiation in terms of dark current and dark counting rate, their temperature dependence and long time behaviour. The irradiated counter efficiency and cluster size were also measured. Visual inspection of different RPC components, the results of SEM, XPS, foil-ERDA, RBS, AFM, THz-TDS analysis and resistivity measurements are presented in Chapter 5, 6, 7, 8, 9, 10, 11 and 12, respectively.

Chapter 13 is dedicated to the conclusions.

2. MSMGRPC architecture and laboratory tests before irradiation

The architecture of the double sided (DS) MSMGRPC under investigation is schematically presented in Fig.1. The two halves of the detector are identical and symmetric relative to the central signal strips electrode. Each stack contains six plan parallel resistive electrodes of 0.7 mm thickness, equally spaced by five gas gaps. The size of the gas gaps is defined by the 140 μm diameter nylon fishing line used as spacer. The resistive electrodes are made from low resistivity glass ($\approx 1.5 \cdot 10^{10} \Omega \cdot \text{cm}$). The outermost glass plates of each half are in contact with the Cu strips of the cathode electrodes while the central 2 glass electrode are in contact with the Cu strips of the anode electrode. The strips of the HV electrodes have 5.6 mm width and a pitch size of 7.2 mm. The pick-up signal strips have a width of 1.3 mm with a pitch size of 7.2 mm, as for the HV electrodes.

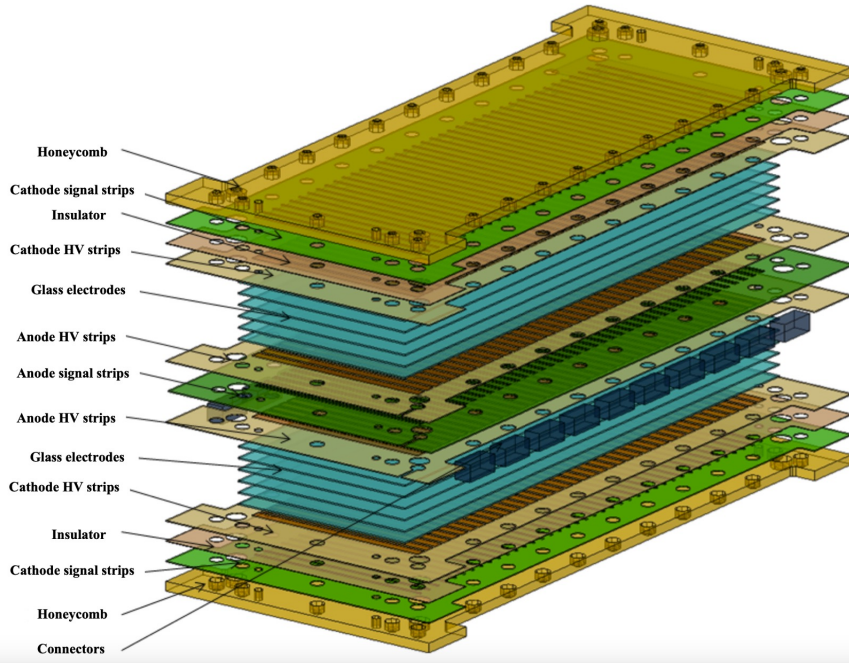


Figure 1: Schematic architecture of a double sided MSMGRPC.

The readout strips behind the corresponding anode and cathode HV ones define a signal transmission line of which impedance depends on the strip width and the properties of the whole structure in between. The signals are readout in a differential mode, both, the anode and the cathode signals, being fed into the input of a readout electronics channel, as can be found in Ref. [12]. For efficiency and time resolution measurements using cosmic rays, a single sided (SS) MSMGRPC was assembled. The glass electrodes, HV electrodes, signal read-out printed circuits are identical with the ones described above. The counter has 10 glass plates and 8 gaps of 140 μm each, arranged in a single stack. The HV

electrodes being only on top and bottom of the structure, in order to reach the same performance in term of efficiency and time resolution, the operating voltage is 2×9 kV relative to 2×5.5 kV for the double sided configuration. This two counters, mounted in a light electromagnetic screened box, were successfully tested in house using cosmic rays and in-beam at CERN-SPS with ionising particles produced by a 30 A·GeV Pb beam on Pb target. A 62 ± 3 psec system time resolution and efficiency of $\approx 97\%$ have been obtained [17]. The final, mandatory test before starting building an important zone of the CBM ToF, i.e. $15m^2$ in the region of the most forward polar angles, is the behaviour of such detectors in high irradiation dose. Simulations based on UrQMD model and FLUKA and GEANT3 transport codes [18] show that for an Au beam with kinetic energy of 10 A·GeV and an intensity of 10^8 ions/sec on fixed Au target over 2 months period, a ionising dose of ~ 500 Gy and a non-ionising dose of $\sim 3 \cdot 10^{11} n_{eq}/cm^2$ is accumulated in the most inner zone of the CBM ToF. Therefore, we started ageing tests of the MSMGRPC described above, using the multipurpose irradiation facility (IRASM) of IFIN-HH [19] where a gamma and X-ray doze rate of 0.3 kGy/h, uniform distributed in the area of exposure, can be accessed.

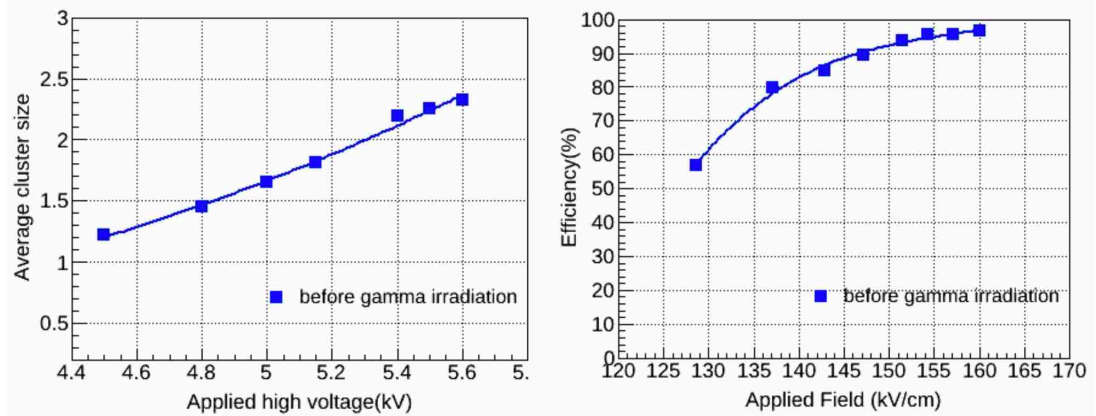


Figure 2: Efficiency (left) and cluster size (right) for cosmic rays tests before irradiation.

Before starting the irradiation, the DS MSMGRPC counter was tested in the detector laboratory of Hadron Physics Department (HPD) of IFIN-HH with cosmic rays. The counter was disassembled, the glass were carefully cleaned and assembled back, the spacers being arranged along the strips in order to enhance the gas exchange rate through the gaps. 16 strips of each of the two RPCs, SS (8 gas gaps, $140 \mu m$ size each) and DS (2x5 gas gaps, $140 \mu m$ size each), were equipped with fast amplifiers based on NINO chip [20] and V1290A CAEN TDCs. The housing box of $\approx 13.5l$ was flushed with $90\%C_2H_2F_4 + 5\%SF_6 + 5\% C_4H_{10}$ gas mixture with a rate of 4 liters/hour. Two plastic scintillator bars of $1.5cm \times 1.5cm \times 10cm$ where used as trigger in different experimental configurations. The results in terms of efficiency and cluster size are presented in Fig.2. The values as a function of the applied high voltage obtained in the previous in-house tests are reproduced. At the working voltage, i.e. 5.6 kV, the measured dark current was bellow 1 nA while the dark counting rate $\approx 1-2$ Hz/cm².

3. Irradiation cave and experimental setup

The experimental setup was transported and installed in the irradiation cave. In Fig.3 left photo can be seen the position of the RPC in the cave. The housing box was aligned (right side, near to the wall) relative to the slit in the concrete protection of the ^{60}Co source where it is lifted up from the water pool underneath (left side). Long pipes for circulating the working gas mixture, HV and signal cables for monitoring the direct signals from the RPC were used to connect the RPC to the gas mixer, HV units and oscilloscope placed in a protected area, nearby the control room of the installation (right photo of Fig.3). Once the ^{60}Co source was lifted in the working position, the HV was switched on and slowly increased, carefully monitoring the current and signals on the oscilloscope, mainly to avoid potential micro-discharges.



Figure 3: Left photo - irradiation cave, the slit in the middle of the concrete shielding (left) and the MSMGRPC in the housing box (right) equipped with gas transport pipes, HV cables and a signal cable for monitoring the signals directly from the counter; Right photo - the gas mixer, HV units and the oscilloscope placed in a protected area, nearby the control room of the installation.

As expected (see Fig.4 left), above 3.5 kV the current abruptly increases. We decided to stay at 4.5 kV in order to avoid some micro-discharges observed above this voltage. At 4.5 kV the counter efficiency is already in the region of 60% (see Fig.2 right)

Once we reached this voltage we started to monitor the current as a function of time. Presented in Fig.4-right, the current increases with the exposure time. After 2 hours of irradiation, a tendency towards levelling off is observed. These plots were obtained during the first irradiation period, a bit longer than 3.5 hours.

The sequence and duration of operating the counter in high irradiation zone, the current, the corresponding charge and accumulated irradiation dose can be followed in Table 1. The total cumulated irradiation dose with HV applied on the counter was 12.99 kGy. One has to mention that the total dose during the irradiation slot, including also the periods when the HV was off but the gas flow on, was of 76.7 kGy.

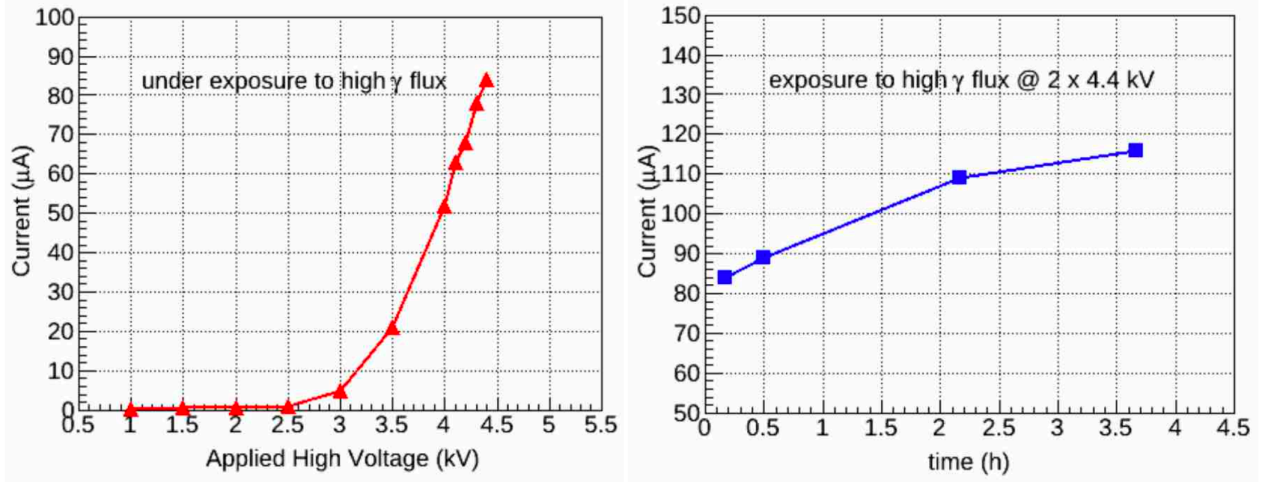


Figure 4: Left - current as a function of applied voltage; Right - evolution of the current with the irradiation time.

4. Post irradiation tests

Once the irradiation period ended and the cave was accessed, the counter and the gas mixer were transported back in the detector laboratory of HPD and prepared for detailed tests. The dark current as a function of measured time and room temperature can be followed in Fig.5. One could see that at 22 hours after the irradiation, the dark current at 5.5 kV, the value which corresponds to an efficiency better than 95% is about three orders of magnitude lower than the values measured during the irradiation periods.

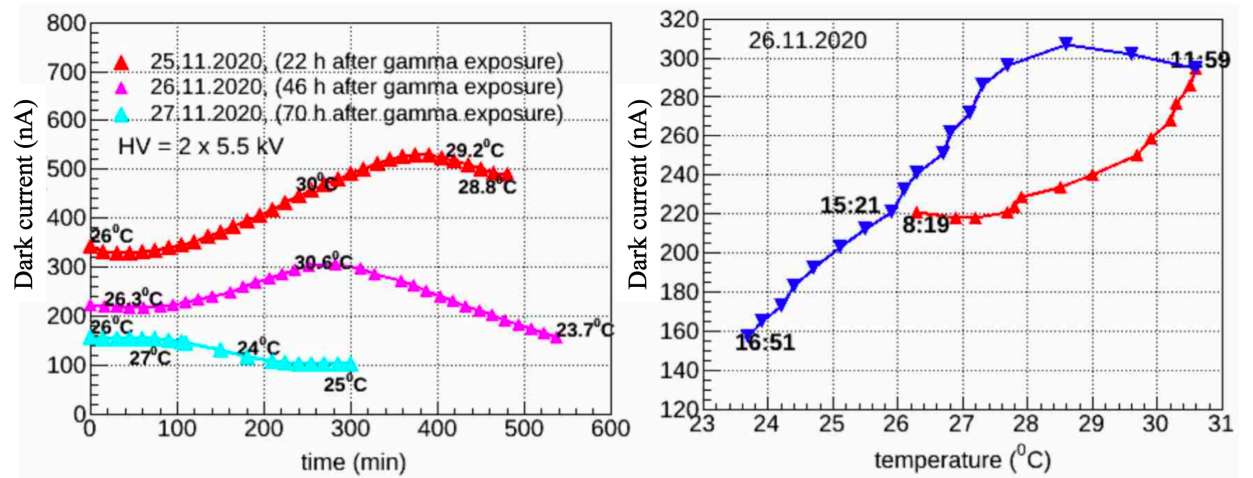


Figure 5: Left - dark current for different periods after irradiation as a function of measured time. The room temperature at different times periods during the measurement could be followed on the three sets of measurements; Right - Evolution of the dark current as a function of room temperature. The time evolution of the temperature during the measurement is marked on the plot at different periods.

It is also evidenced a temperature dependence of the dark current, stronger than the one specific for a nonirradiated

counter. The average value and time dependence of the dark current decrease with time elapsed since irradiation. The evolution of the dark current and dark counting rate on a long period is presented in Fig.6. In two weeks after the irradiation their values converged towards those measured before the irradiation. A similar trend was observed in a long term change of electrical conductance at room temperature in air of a fluorine graphite fiber intercalation compound [21].

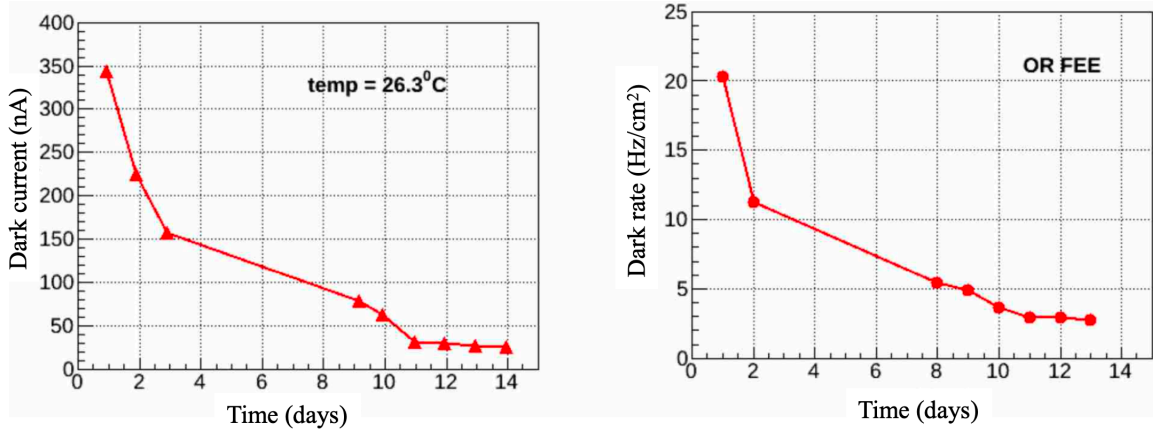


Figure 6: Left - dark current; Right - dark counting rate evolution with time after the irradiation. The counter was operated at nominal voltage.

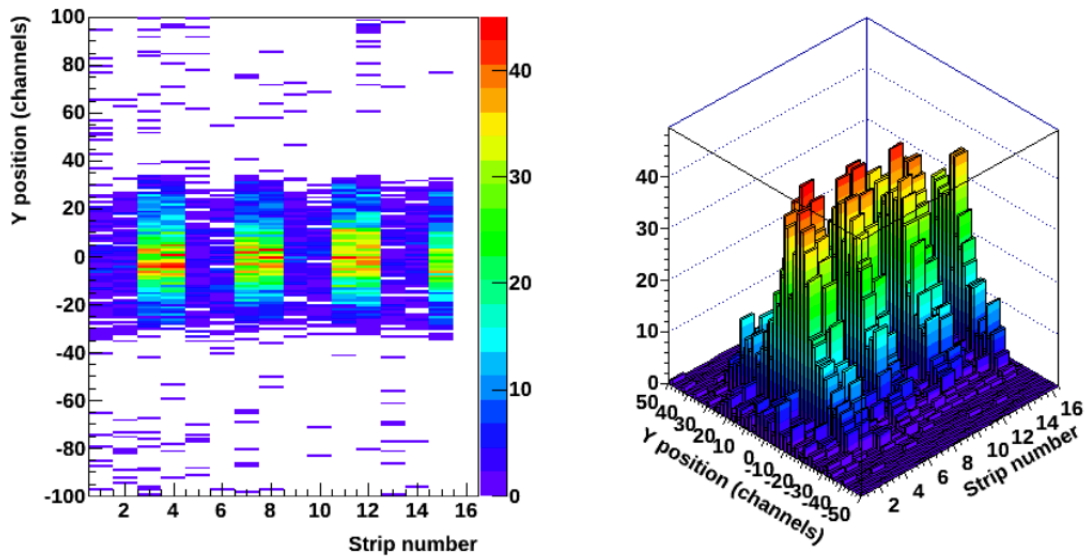


Figure 7: Left - position along the strip versus strip number; Right - the same in a 3-dimensional representation obtained with random coincidence with SS-MGMSRPC.

Based on the time difference between the two ends of the 16 operated strips, the position along the strips (y) was reconstructed. A two and three-dimensional representations of the position along the strips versus strip number, obtained as random coincidences with SS-MGMSRPC, is presented in Fig.7.

Ageing tests of MSMGRPC in high irradiation dose

Date (dd/mm)	Duration (hours)	I (μ A)	< Q > (C)	Doze rate (kGy/h)	Cumulated dose (kGy)
10.11	3:30.	105	1.4175	0.3267	1.225
11.11	2:30	125	1.125	0.3267	2.096
12.11	3:00	106	1.1448	0.3267	3.076
13.11	3:00	168	1.8144	0.3267	4.056
16.11	3:20	289	3.468	0.3222	5.130
17.11	3:30	363	4.5738	0.3222	6.258
18.11	6:35	254	6.0198	0.3222	8.379
20.11	4:00	397	5.7168	0.3145	9.637
23.11	3:10	233	2.6562	0.3145	10.633
23.11	3:00	288	3.1104	0.3145	11.577
24.11	4:30	246	3.990	0.3145	12.992
	40:33		35.0367		12.992

Table 1

Date, irradiation duration, MSMGRPC current, total accumulated charge, irradiation dose rate and cumulated irradiation dose during the irradiation tests.

A clear enhanced activity in the adjacent strips, left-right, to the spacers positioned in between them, is evidenced.

Using cosmic rays and a coincidence condition between the single sided MSMGRPC, exposed to the irradiation dose without HV on, and one of plastic scintillator bars, such that the double sided MSMGRPC under investigation to be sandwiched by them, two-dimensional plots y vs. strip numbers for the two MSMGRPC were obtained. They are presented in Fig.8. It is clearly seen that the coincidence condition with the plastic scintillator removes the activity within the spacers regions and a rather uniform distribution of the hits produced by cosmic rays on the surface of the MSMGRPC under investigation is obtained.

The resulting values of the efficiency and cluster size for the MSMGRPC operated in high irradiation dose are represented by red squares in Fig.9. The blue squares represent the corresponding values before the irradiation. Within the symbols size, no change in the efficiency after the irradiation is observed. A decrease in the cluster size by 25% is observed. This could be explained by a decrease of the signals after irradiation, still above the FEE threshold value for the strips corresponding to the centroid of the avalanche but bellow the threshold value for the neighbouring strips.

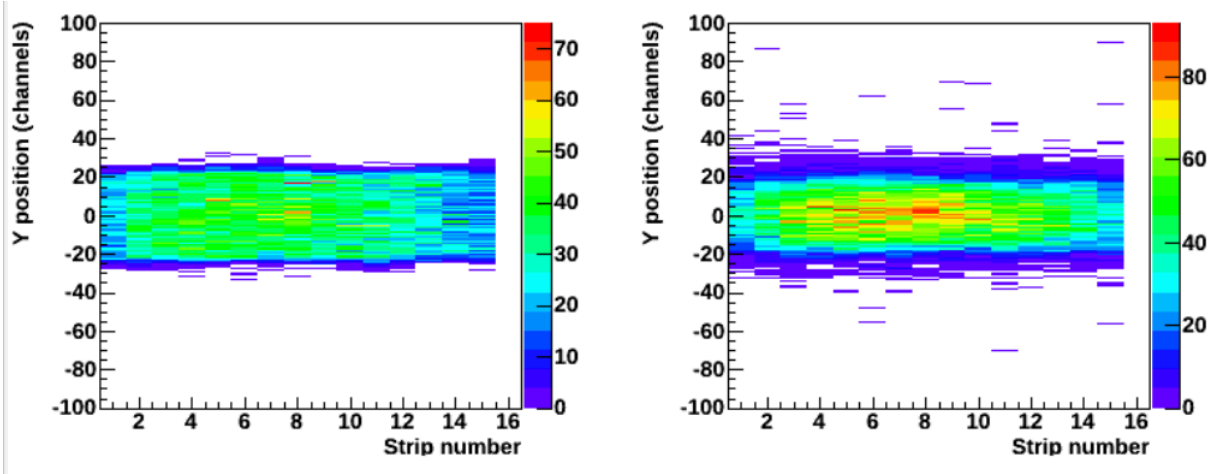


Figure 8: Cosmic ray tests: Left - position along the strip versus strip number for the irradiated double sided MSMGRPC; Right - position along the strip versus strip number for a non-irradiated single sided MSMGRPC used in coincidence with a plastic scintillator as a trigger.

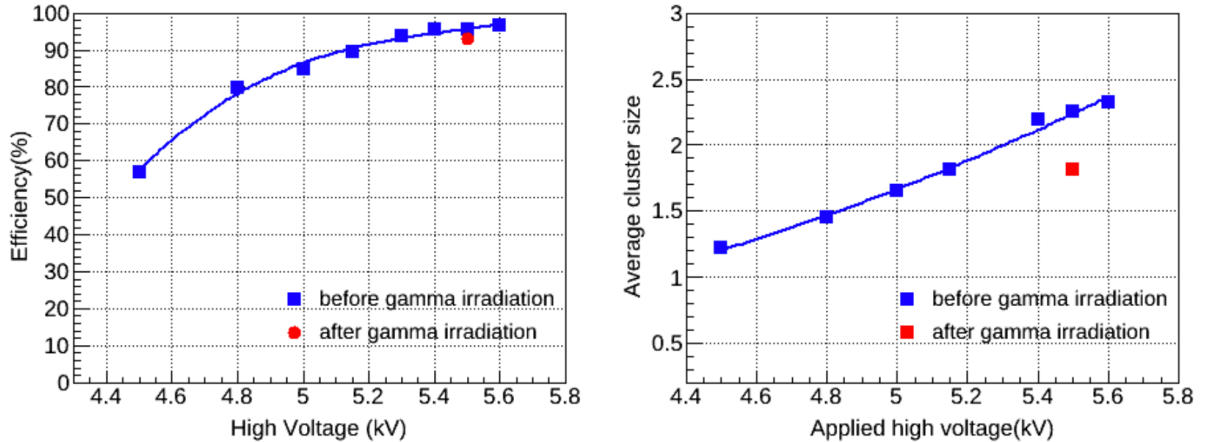


Figure 9: Left - efficiency; Right - cluster size - red squares compared with the values before the irradiation - blue squares.

5. Visual inspection after the irradiation

After the tests described in the previous chapter, the housing box was opened for a visual inspection of the ageing effects on different detector components. Before disassembling the MSMGRPC, a general inspection showed that plastic screws, the honeycomb plates used to sandwich the counter for a mechanical stability, gas pipes and the epoxy used to seal the HV, signals and gas connections through the aluminium back flange got yellowed, see Fig.10. The gasket used for gas tightness of the housing box became rigid. No impact of these changes on the mechanical properties or detector functionality was observed.

Once the MSMGRPC structure was disassembled we accessed the floating glass electrodes and start the inspection. In the photos from Fig.11 could be seen the two sides of a glass floating electrode. The surface facing the cathode

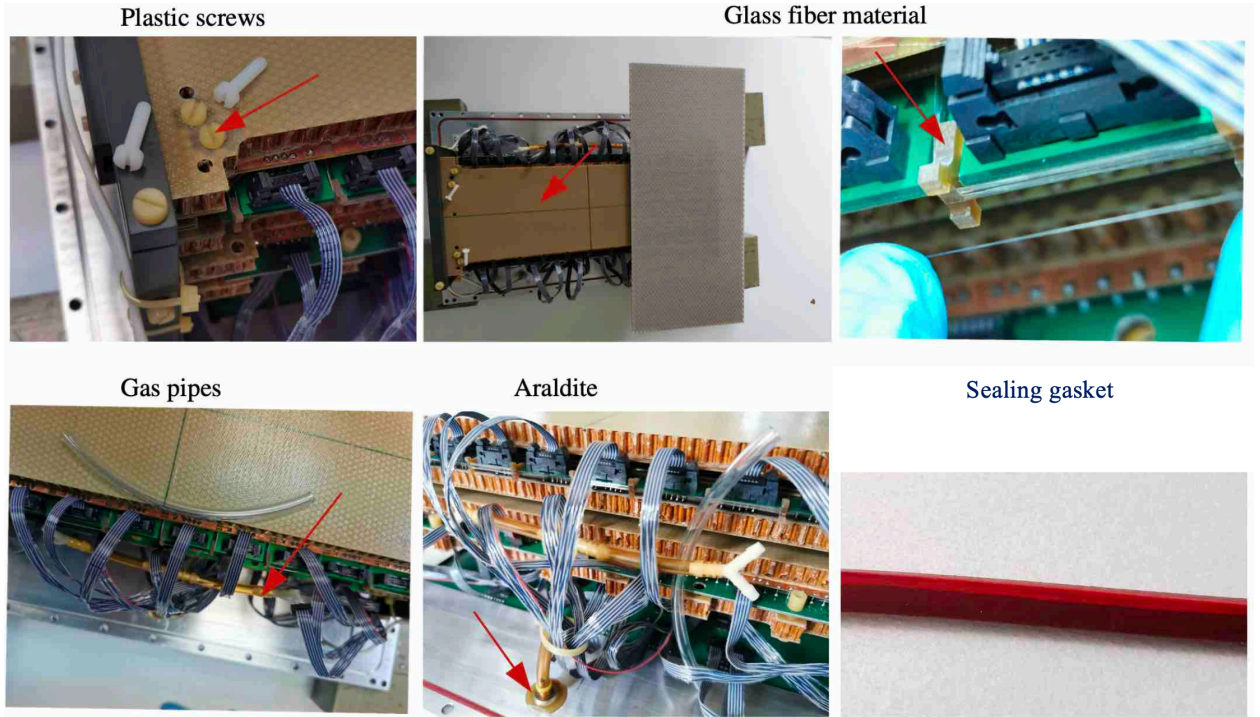


Figure 10: Photos of plastic screws, honeycomb plates used to sandwich the counter for mechanical stability, gas pipes compared with non-irradiated ones, the epoxy used to seal the HV, signals and gas connections through the aluminium back flange and the sealing gasket.

electrode is presented in the upper photo and the surface facing the anode electrode in the bottom one. For simplicity, for the rest of the paper we used the label anode for the surface of the glass phasing the cathode and cathode for the surface of the glass phasing the anode. A clear difference, in terms of colour and quantity of the deposited layers, is observed. The more consistent and colourful deposited layer seems to be on the anode surface. The strip type pattern corresponds to the strip structure of the two high voltage electrodes. All floating glass electrodes present similar characteristics independent on their position within the stack. One can also observe less deposition at the edges of the glass electrode where a better gas exchange via diffusion in the gaps region takes place. A closer view of the two surfaces taken with a normal microscope evidenced details of the deposited layers. In Fig.12 are shown regions around the spacers. The left photo corresponds to the anode surface and the right photo corresponds to the cathode surface. It is observed that in the region of spacers, where the highest dark counting rate was observed, the deposition is enhanced. Unexpected thinner horizontal trace in the right photo, cathode surface, is evidenced. It corresponds to the position of the previous spacer, orthogonal to the high voltage strips, used in the tests before ageing studies. For a better gas exchange in the gas gaps region we decided to position the spacers along the HV strips, in the gap region between two adjacent strips. The counter was disassembled, the glass plates were carefully cleaned, no trace along the previous longitudinal spacers being observed after. The counter was reassembled for ageing tests, using the same glass

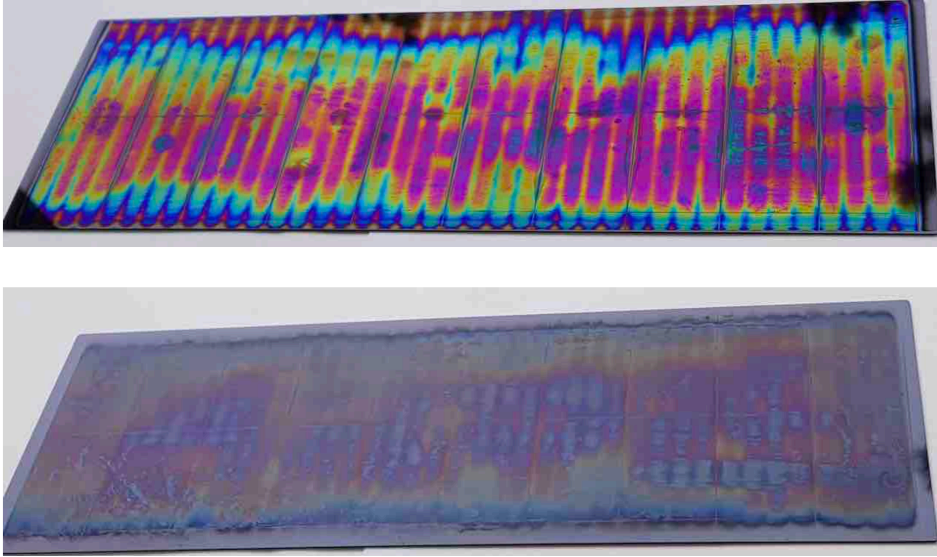


Figure 11: Photos of one of the glass floating electrodes: Top photo - surface facing the cathode (anode): Bottom photo - surface facing the anode (cathode).

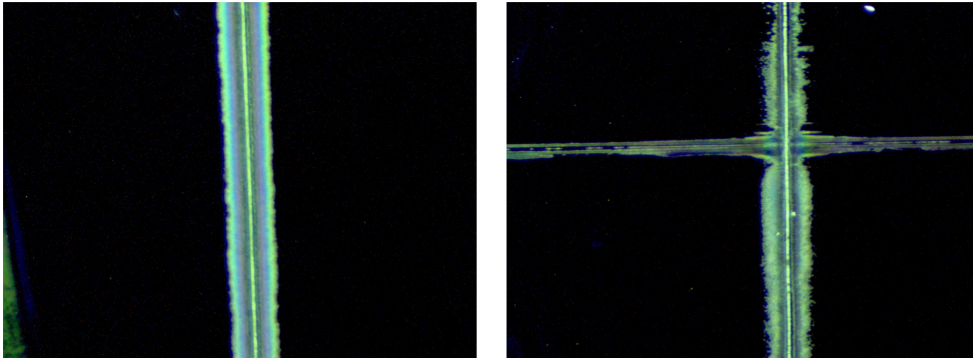


Figure 12: Photos of the regions around the spacers: Left photo - anode surface; Right photo-cathode surface.

plates after being cleaned. In Fig.13 are presented photos taken in different regions of the cathode surface of the glass electrode. Besides irregular deposition spots, regular straight thin lines or ring shape patterns are evidenced. Quite probable this is the result of hydrogen fluoride radical, produced in a polymerisation process in highly dense streamers environment, which develops latent very fine patterns [22], already existing on the glass plates before irradiation. While the deposited layer on the anode surface can be easily removed using ethyl alcohol, the clean spot in the left photo of Fig.14, the deposited layer on the cathode surface of the glass electrode can not be removed using distilled water, ethyl alcohol or acetone. The continuous layer can be removed mechanically using a fine scalpel, resulting fine white powder, see the right photo of Fig.14. However, in the cleaned area remains a spot which seems to be a kind of crater in the glass electrode, quite probable the result of an ablation process. After this visual inspections we decided to use different analysis methods in order to find the elemental and chemical composition of the deposited layers, their

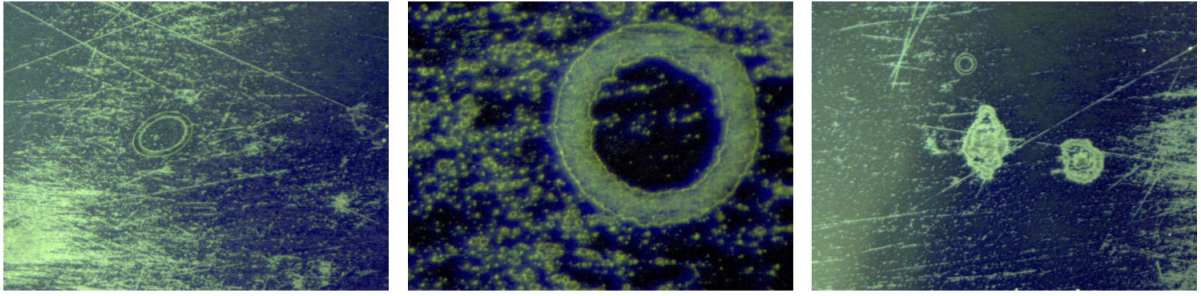


Figure 13: Photos of different regions of the cathode surface of glass electrode.

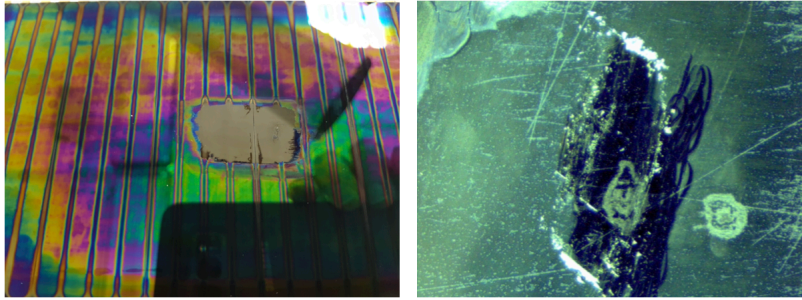


Figure 14: Photos of one of the floating electrodes: Left - cleaned portion of the anode surface using ethyl alcohol; Right - removed deposited layer on the cathode surface using a scalpel.

roughness and electrical properties of the glass electrodes of the irradiated MSMGRPC relative to a non-irradiated glass electrode. The results are presented in the following chapters.

6. SEM analysis

A scanning of the deposited layer structure with higher resolution was done using a Scanning Electron Microscope (SEM). Samples of some of the obtained images with two different resolutions are presented in Fig.15. The left column corresponds to the cathode surface of the glass plate while the right column to the anode surface. A clear difference in the structure of deposited layers is evidenced. More regular structures correspond to the cathode surface. A higher resolution image, bottom row, evidence irregular spots on the anode surface. Similar scanning was done for a non-irradiated glass plate and the results are presented in Fig.16. While by naked eye such zones hardly could be spotted, with SEM method one could observe regular patterns, ring or disc type which clearly shows that they have a crystalline structure. Such local structures were also observed in Pestov type low resistivity glass [23] and expected to be produced during the rather complex production process, rather different than the one used for commercial float glass production.

Further Energy-Dispersive X-ray Spectrometry (EDX) investigations on the elemental composition of some samples of surfaces were done and the results are presented in the top plots of Fig.17 and Fig.18 for a non irradiated glass and for the anode and cathode surfaces of a glass electrode after irradiation of MSMGRPC, respectively. The EDX

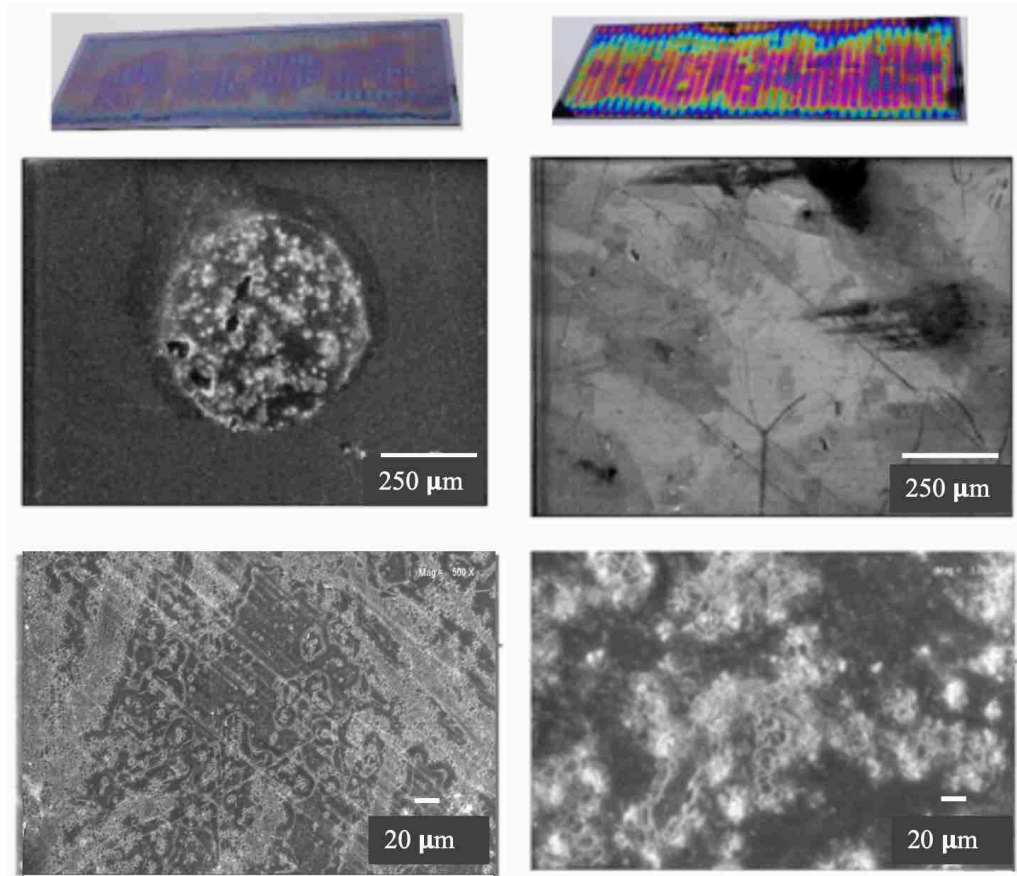


Figure 15: Samples of SEM images of one of the floating electrode surfaces: Left column - the anode surface; Right column - the cathode surface.

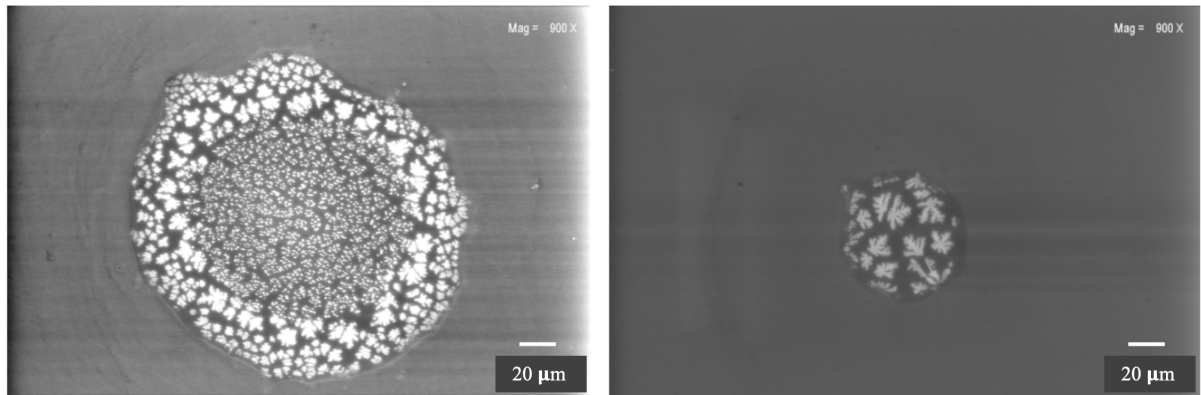


Figure 16: Magnified two regions of a not irradiated glass plate.

analysis was done in standard less mode. The relative content of different components are listed in bottom tables of each figure. The elements found by analysing the surface of a not exposed glass plate confirm the elemental composition reported by the producers, i.e. SiO_2 , Fe_2O_3 , Na_2O , Al_2O_3 , MnO_2 [24] with the exception of Mn. The lack of

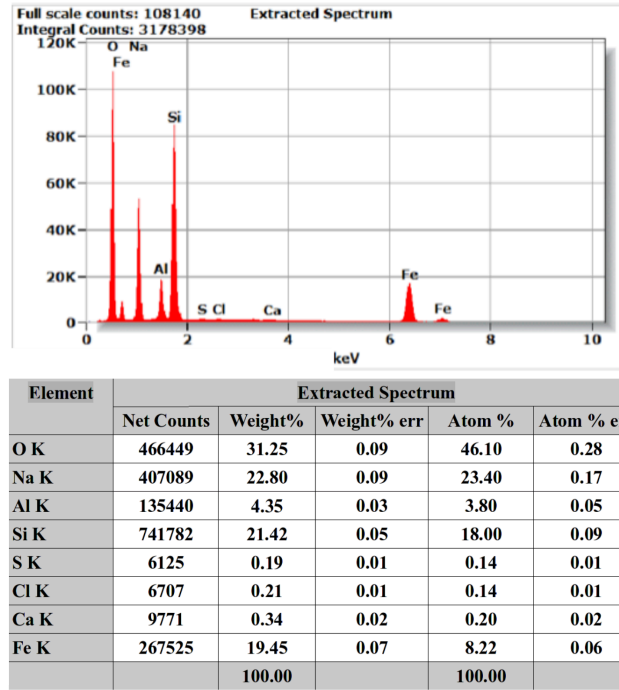


Figure 17: Top: electron spectra corresponding to the surface of the non-irradiated glass plate; bottom: the corresponding relative elemental composition.

manganese from EDX spectra can be explained by the fact that the amount in the samples is below the detection limit of $\approx 1,000$ ppm. As far as concerns the relative percentage presented in Fig.17 of the present analysis, they can not be confronted with the producer's values as far as they were not reported in the literature.

However, a definite conclusion is that the not exposed glass plates do not have any fluorine content. The fluorine percentage on the surface of glass electrodes used in the MSMGRPC operated in high irradiation dose is significant and different for the two surfaces. The anode surface contains $31.73 \pm 0.3\%$ fluorine relative $18.81 \pm 0.2\%$ found on the cathode surface. As far as concerns the oxygen content, relative to $46.10 \pm 0.3\%$ corresponding to not irradiated glass plate, the values obtained for the irradiated glass plate are $23.12 \pm 0.2\%$ and $36.42 \pm 0.3\%$ for the two surfaces, respectively. For the rest of elements, no significant difference is evidence between the irradiated and non-irradiated glass plates. One should consider that due to a rather large non-uniformity in the deposited layer on the two surfaces of the irradiate glass, the results of the above measurements are position dependent. The analysis was performed in variable pressure secondary electrons (VPSE) mode at 20 Pa and 20 kV voltage for accelerating the electron beam. The probe current was 700 pA at a working distance (WD) of 14 mm using different magnifications: x100, x250 and x1,000. A scanned area of $\approx 1.2 \text{ mm}^2$ and a penetration depth of $4 \mu\text{m}$ were used for the EDX spectra. The results of the SEM investigations performed on glass sample cross section, the glass being cut in several regions and placed at 90° orientation in the SEM microscope, are presented in Fig.19. An average variation of 50% and in some particular

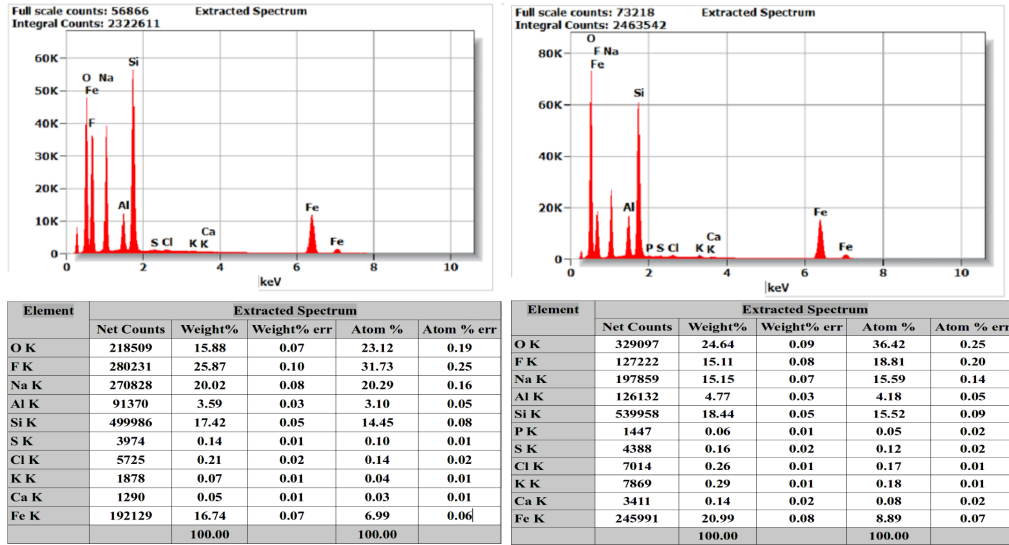


Figure 18: Left-top: electron spectra corresponding to anode surface of irradiated glass; Left-bottom: the corresponding relative elemental composition. Right-top: electron spectra corresponding to cathode surface of irradiated glass; Right-bottom: the corresponding relative elemental composition.

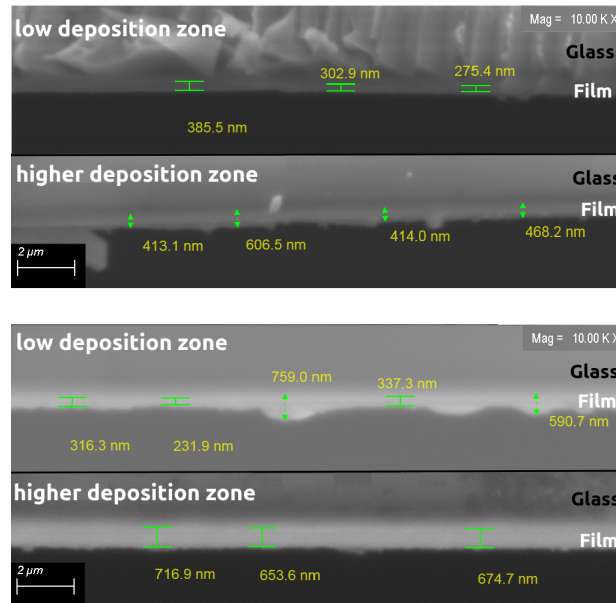


Figure 19: Top: cross-section scanning of the cathode surface in two regions with different deposition thickness, i.e low deposition and higher deposition; Bottom: cross-section scanning of the anode surface.

regions up to a factor of two in the deposited layer is observed. As preliminary optical inspection also suggested, the deposition on the anode surface is considerably thicker than the one deposited on the cathode surface.

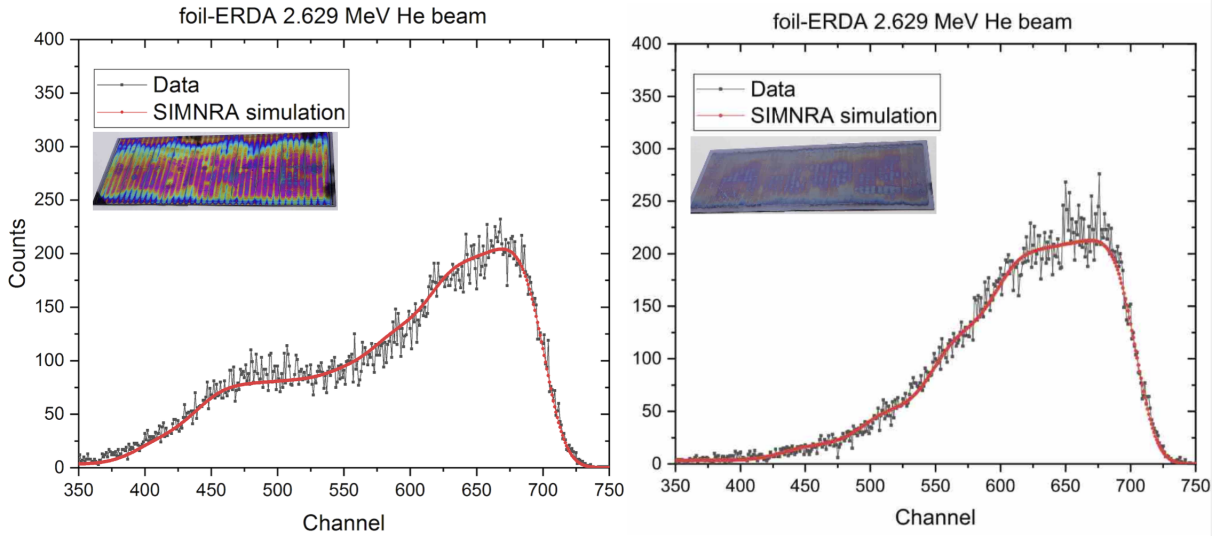


Figure 21: ERDA measurements of hydrogen distribution for the two surfaces of an exposed glass electrodes. ERDA spectra collected with the detector solid angle of 1 msr and the total charge of 1.8 μC : Left-anode surface; Right-cathode surface. The channel vs. counts spectra can be converted to a depth scale (10^{15} atoms/ cm^2) vs. H concentration (%) plot using SIMNRA code. H concentration values and their depth profiles are given in Tables 2 and 3.

Layer	C	H	F	Si	Al	Na	Thickness (10^{15} atoms/ cm^2)
1	0.43	0.18	0.282	0.05	0.01	0.048	675
2	0.32	0.17	0.297	0.05	0.01	0.153	675
3	0.2	0.135	0.407	0.05	0.01	0.198	555
4	0.18	0.085	0.417	-	0.01	0.198	400

Table 2

Relative percentage of elemental content of different layers (first column) and corresponding thickness (last column) for the deposition on the anode surface of the glass plate.

to the beam. The incident beam angle and the exit angle as measured from the normal to the sample surface were both 75° . The 12 μm thick MylarTM stopping foil were located in front of the ERDA detector to separate hydrogen recoils hitting the ERDA detector from scattered He ions. The RBS and foil-ERDA spectra were simulated using SIMNRA software package version 7.02 [26]. The accumulated charge for each RBS spectrum was 10 μC while for foil-ERDA was 1.8 μC . The measurements were performed using a low beam density current, the intensity for the electrical current was about 4 nA and the beam spot of around 1.5 mm in diameter.

As it is known, this method gives access to a profile of the elemental contribution in different layers in the deposited material. The thickness of different layers is given in thin film unit (TFU) and the layers are labeled from 1 to 4(5) starting from the surface. The results are presented in Tables 2 and 3. The areal density, or thin film units, are the natural units for ion beam analysis, since the energy loss is measured in $\text{eV}/(\text{atoms}/\text{cm}^2)$ and the monolayer is of the order of 10^{15} atoms/ cm^2 [27, 28]. Fluorine is present on both surfaces. The content of fluorine on the cathode surface is lower and constant as a function of depth in the deposited layer, relative to the content in the deposited layer on

Layer	C	H	F	Si	Al	Na	O	Fe	Thickness (10^{15} atoms/ cm^2)
1	0.085	0.19	0.056	0.1	0.05	0.212	0.202	0.105	675
2	0.01	0.19	0.056	0.183	0.05	0.185	0.236	0.09	675
3	-	0.13	0.056	0.182	0.05	0.187	0.304	0.09	555
4	-	0.06	0.056	0.0182	0.05	0.188	0.374	0.09	555
5	-	0.026	0.056	0.182	0.05	0.188	0.408	0.09	555

Table 3

Relative percentage of elemental content of different layers (first column) and corresponding thickness (last column) for the deposition on the cathode surface of the glass plate.

the anode surface where the amount is increasing going deeper in the deposition. Contrary to the anode surface, the cathode one contains important percentage of oxygen, increasing with depth. The carbon content is reversed, i.e. the cathode layer has rather negligible amount of carbon in the superficial layer while the percentage of carbon in the anode layer is high, decreasing going deeper in the deposited layer.

9. RBS analysis

Non-Rutherford Backscattering Spectrometry (NRBS) using 3.04 MeV and 4.28 MeV He beams were performed to determine the thickness and stoichiometry of the samples. A Si detector was placed at 165° with respect to the beam direction. The energy resolution of the experimental setup was about 18 keV. In order to quantify the presence of light elements (C and O) in the sample we have used 3.04 MeV to take advantage of the high cross-section of ^4He with oxygen and 4.28 MeV with carbon. The results are presented in Fig.22.

These results confirm the higher content in oxygen of the deposition on the cathode surface and larger fluorine content on the anode surface. The missing Fe component on the cathode surface, which enters in the composition of the glass electrode could be explained by the larger thickness of the deposited material. A precise carbon composition of the non-irradiated glass plate and the two surfaces of the irradiated one is obtained. The results are presented in Fig.23 where the corresponding three spectra are overlapped. These results confirm that the largest carbon content is in the deposited layer on the anode surface, negligible amount being observed on the surface of non-irradiated glass. The uncertainty in RBS and foil-ERDA data analysis is about 5% and 8%, respectively.

10. AFM analysis

Using atomic force microscopy (AFM), one could obtain information on the surface roughness in three dimensions, giving information on the surface morphology [29, 30, 31]. In order to access a better resolution for the present analysis we used tapping mode. A MultiMode Nanoscope IIIA Controller was used for the measurements [31]. The measurements were done at the room temperature and a RTESP (Phosphorus (n) doped Si) cantilever with an elasticity constant of 20-80 N/m. For data acquisition and off-line data processing AFM NanoScope v531r1 software

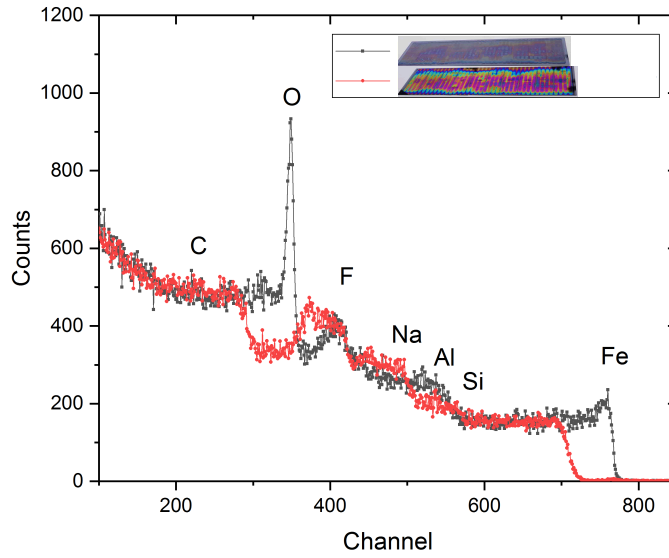


Figure 22: RBS spectra corresponding to the two surfaces of irradiated glass plate overlapped: Black colour corresponds to the cathode surface, Red colour corresponds to the anode surface.

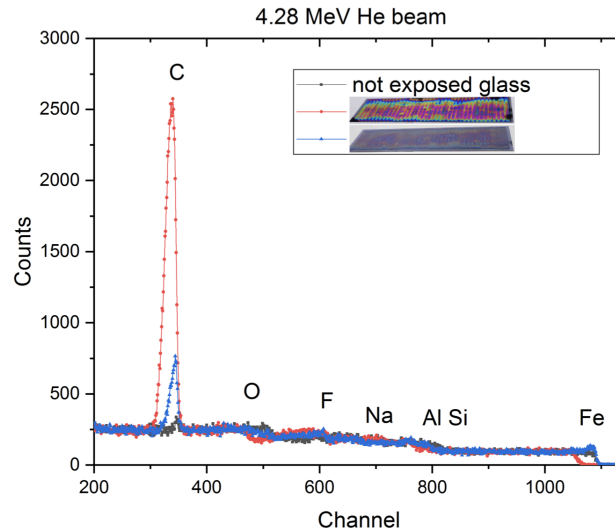


Figure 23: Overlapped ^{12}C - ^4He resonance spectra for: black colour - not irradiated glass plate; blue - the cathode surface; red - the anode surface, respectively.

environment was used.

A 3D representation of a $5 \times 5 \mu\text{m}^2$ scanned surface of a non-irradiated glass plate is presented in Fig.24 left. Projections on one axis following the three coloured lines shown in middle of Fig.24 can be followed on the right plot. The observed structures with a peak to valley difference of 10-40 nm are more or less at the same level as those reported in [24].

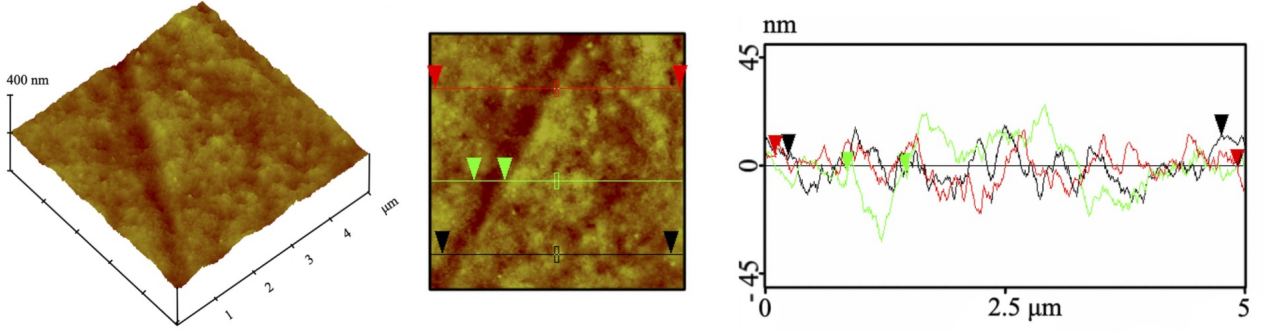


Figure 24: Left-3D representation of a $5 \times 5 \mu\text{m}^2$ scanned surface of a non-irradiated glass plate; Middle-2D projection of the 3D plot; Right-projections on one axis following the three coloured lines shown in the middle plot.

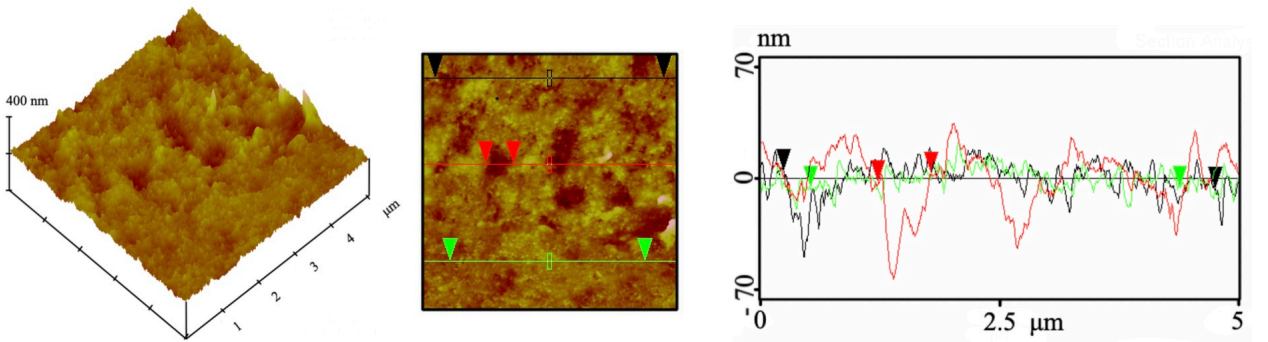


Figure 25: Left-3D representation of a $5 \times 5 \mu\text{m}^2$ scanned surface of an irradiated glass plate in the red-brick region of the anode surface; Middle-2D projection of the 3D plot; Right-projections on one axis following the three coloured lines shown in the middle plot.

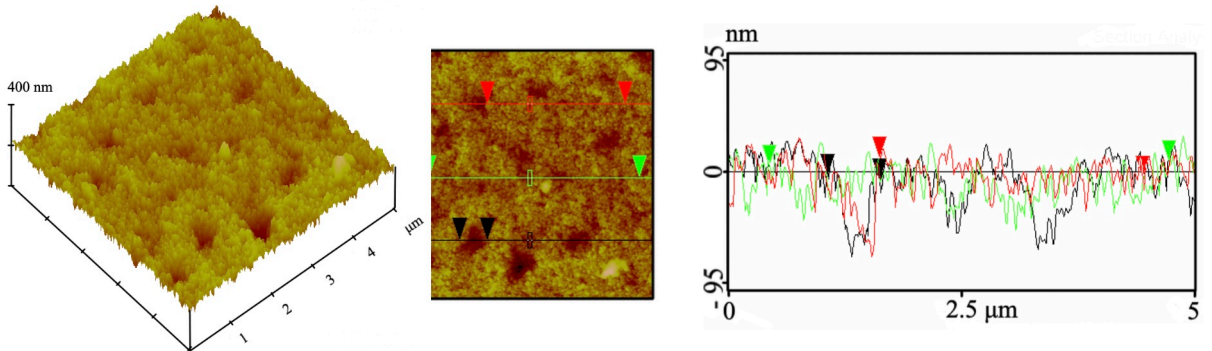


Figure 26: Left-3D representation of a $5 \times 5 \mu\text{m}^2$ scanned surface of an irradiated glass plate in the greenish region of the anode surface; Middle-2D projection of the 3D plot; Right-projections on one axis following the three coloured lines shown in the middle plot.

The results for a red-brick region on the anode surface of the exposed glass plate are presented as 3D, 2D and uni-dimensional plots in Fig.25. More pronounced structures are evidenced, the peak to valley differences being up to the level of 100 nm.

The results for a greenish region on the same side of the exposed glass plate are presented in Fig.26. The peak to

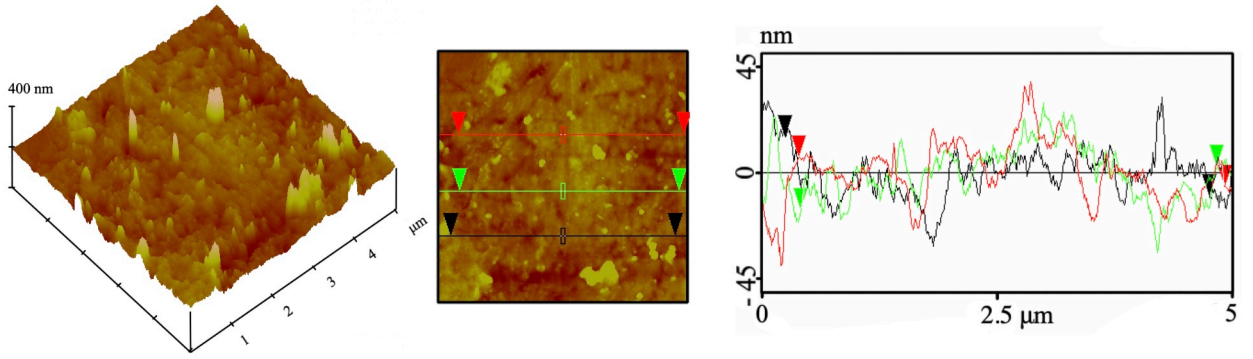


Figure 27: Left-3D representation of a $5 \times 5 \mu\text{m}^2$ scanned cathode surface of an irradiated glass plate; Middle-2D projection of the 3D plot; Right-projections on one axis following the three coloured lines shown in the middle plot.

valley differences are similar with those observed for the red-brick region.

In Fig.27 are presented the results for the cathode surface of the irradiated glass electrode. Sharp peaks, randomly distributed are evidenced, the peak to valley differences being up to the level of 70-80 nm in the scanned region.

11. THz-TDS analysis

As it is known, the terahertz time-domain spectroscopy (THz-TDS) is used to determine the optical and dielectric constants of a given material. Therefore, we used this method to study the changes in the refractive index and real and imaginary dielectric constant of the floating glass electrodes used in the MSMGRPC operated in high irradiation dose.

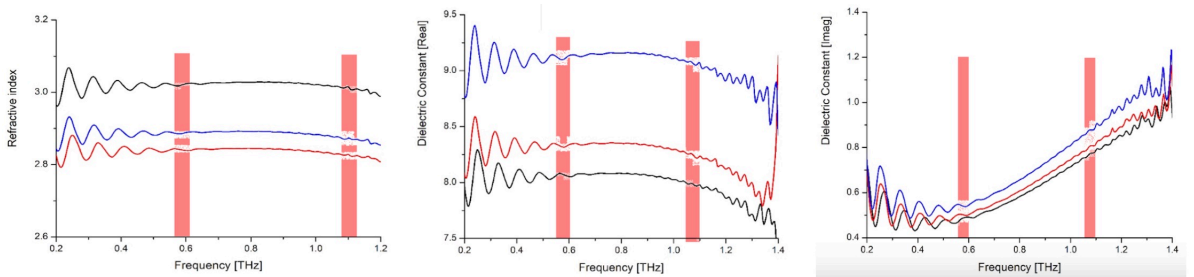


Figure 28: From left to right: refractive index, real part of dielectric constant and imaginary part of the dielectric constant; black curves - not irradiated glass plate, red curves - the cathode surface and blue curves - anode surface. The measurement with the highest accuracy is between the orange vertical stripes.

The results are presented in Fig.28. A decrease of the refractive index of $\approx 5.8\%$ is observed for the irradiated glass plate relative to the one not exposed to the radiation. The refractive index of the cathode layer is a bit lower relative to the anode layer. The dielectric constant, real and imaginary components are by $\approx 10\%$ lower for the surfaces of the exposed electrodes relative to the values corresponding the non-irradiated glass plate.

In Fig.29 are presented the variation of the real and imaginary parts of the dielectric constant with frequency cor-

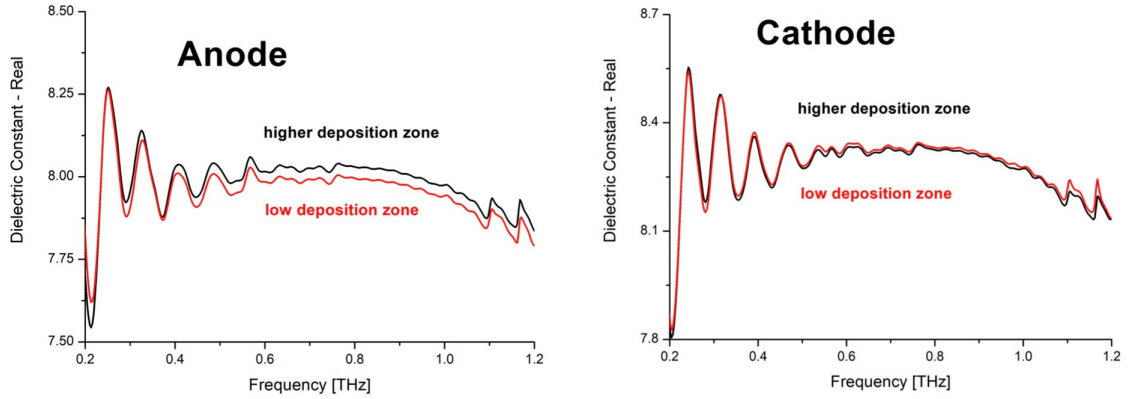


Figure 29: Left: real part of the dielectric constant for the anode surface of the glass electrode (Anode) in two regions: higher deposition and low deposition zones. Right: real part of the dielectric constant for the cathode surface of the glass electrode (Cathode) in two regions: high deposition and low deposition.

responding to zones with different thickness of the deposited material on the two surfaces of a floating glass electrode. Based on the statistics of the thickness variation between low and high deposition areas, both for anode and cathode glass surfaces and correlating them with the dielectric constant variation presented in Fig.29, one could have a qualitative assessment about the influence of the deposited layers on the electrode capacity variation. A capacity variation of about 0.05% per deposited micrometer material is expected for the cathode surface and 0.7% for the anode surface.

The observed changes in the dielectric constants of irradiated floating electrodes on the transmission line impedance is of the order of a few percent, therefore no major impact on the impedance matching to the one of the frontend electronics is expected.

12. Resistivity measurements

An other important diagnose of the impact of high irradiation dose environment on the counter performance concerns the changes of the surface and volume resistivity of the exposed glass electrodes. These measurements were done for the floating glass electrodes and also for the glass plates in direct contact with the strip structured high voltage

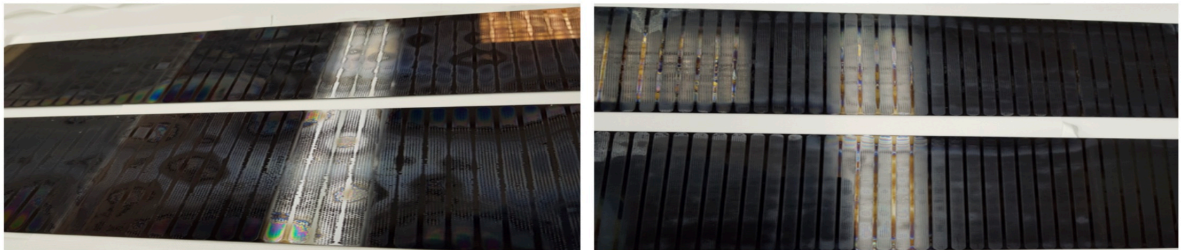


Figure 30: Photos of the two glass electrodes in touch with the strip structured high voltage electrodes: Left: the surface in a direct contact with the cathode electrode; Right: the surface in direct contact with the anode electrode.

Probe	R_V ($G\Omega\cdot cm$)	R_S ($G\Omega/\square$)
irradiated cathode surface	67.4	20.0
irradiated anode surface	61.5	21.1
non-irradiated glass	65.2	20.2

Table 4

Volume (R_V) and surface (R_S) resistivity for the two surfaces of irradiate glass and for non-irradiated glass

Probe	R_V ($G\Omega\cdot cm$)	R_{SA} ($G\Omega/\square$)	R_V ($G\Omega\cdot cm$)	R_{SK} ($G\Omega/\square$)
1	64.6	19.1	62.6	20.8
2	64.3	17.6	60.6	19.4
3	64.0	16.8	58.5	17.5
4	62.1	17.9	61.5	17.3

Table 5

Volume (R_V) and surface (R_S) resistivity for the two surfaces of irradiate glass in contact with anode (SA) and cathode (SK) high voltage electrodes for four different regions on the surface.

electrodes. Photos of the surfaces of glass plates in a direct contact with the high voltage electrodes are presented in Fig.30. In general, the deposition seem to be less than on the floating glass electrodes, showing that most of the deposited material is due to ionisation and recombination of the basic components of the working gas in the gaps between consecutive glass electrodes. The layer on the surface in contact with the cathode seems to be thicker, regular patterns are visible and the edges of the gaps between strips are rather irregular relative to the ones produced on the surface in contact with the anode which are very sharp.

The surface and volume resistivity for a floating glass electrode and for the glass plates in contact with the high voltage electrodes of irradiated MSMGRPC as well as for the non-irradiated glass were measured using a Keithley 6517B Electrometer with 8009 Test Fixture. The results corresponding to floating glass electrodes used during irradiation and to a non-irradiated glass are presented in Table 4. If one considers the position dependence on surface, no major change in the surface and volume resistivity between the irradiated and non-irradiated glass is observed. Similar measurements were performed for four samples taken from different regions of the glass plates in contact with the anode (A) and cathode (K) electrodes. The results presented in Table 5, show that, as in the case of floating electrodes, the surface and volume resistivity are similar with the values corresponding to the non-irradiated glass plates.

13. Conclusions

Detailed studies of the effects of high density avalanches induced by high irradiation dose in a short time on two-dimensional position sensitive timing resistive plate counters are reported. They confirm earlier studies on ablation and polymerisation taking place in low pressure plasma [15] or long term ageing studies in rather moderate irradiation dose [16]. Deposition of different radicals produced by polymerisation on the anode surface of the floating glass electrodes,

with relative weights of different elements as a function of deepness of the deposited layer is evidenced. These layers could be easily cleaned using ethyl alcohol. Fluorine radicals which produce ablation/etching of the cathode surface of glass electrodes are evidenced. Besides a continuous layer, regular patterns are evidenced which could be explained as the results of already existing tiny patterns on the non-exposed glass which are enhanced by ablation/etching process. The surfaces roughness increases relative to the non-irradiated glass. Surface and volume resistivity, dark current, dark counting rate, efficiency and cluster size measurements after irradiation show that there is a recovery process which brings the counter to the initial performance. The present studies were performed using a housing box flashed with the working gas mixture. Therefore, the gas exchange in the $140\text{ }\mu\text{m}$ 10 gas gaps of the counter is via diffusion process. It is well known [15] that the polymerisation phenomena is inverse proportional with the gas flow. A directed gas flow through the gas gaps is expected to decrease the observed ageing phenomena. Such a new architecture is in progress to be realised. Based on the produced charge in the counter during the operation in the high irradiation dose and the charge produced by a minimum ionising particle we estimated more than $3\cdot 10^5$ avalanches/ $\text{cm}^2\cdot\text{sec}$, 10 times higher than the counting rate expected at CBM for the most forward region, i.e. low polar angles. Besides an increase of the gas flow through the gas gaps, an exposure to a lower dose and longer time, conclusive for the operating conditions in CBM experiment, will be performed.

14. Acknowledgments

This work was carried out under the contracts sponsored by the Romanian Ministry of Research, Innovation and Digitalization: CBM FAIR-RO-03 (via IFA Coordinating Agency), PN-19-06 01 03, PN-19-06 03 03, PN-19-06 02 01, UEFISCU - CDI - HIGHkDEVICE, PN-III-P4-ID-PCCF-2016-0175. The ion beam experiments were performed at the 3 MV TandetronTM of IFIN-HH being supported by the "National Interest Infrastructures" Program.

References

- [1] CBM Collaboration, Challenges in QCD matter physics - The scientific programme of the Compressed Baryonic Matter experiment at FAIR, *Eur.Phys.J. A* 53 (2017) 60.
- [2] CBM Collaboration, Technical Design Report, GSI-2015-01999, Time-of-Flight System (2014).
- [3] M. Petrovici et al., A large-area glass-resistive plate chamber with multistrip readout, *Nucl. Instr. Methods A* 487 (2002) 337.
- [4] M. Petrovici et al., Multistrip multigap symmetric RPC, *Nucl. Instr. Methods A* 508 (2003) 75.
- [5] A. Schuetttauf et al., Multi-strip MRPCs for FOPI, *Nucl. Instr. Methods A* 602 (2009) 679.
- [6] M. Kis et al., Multi-strip Multi-gap RPC Barrel for Time-of-Flight Measurements, *Nucl. Instr. Methods A* 646 (2011) 27.
- [7] A. Blanco et al., Performance of the HADES-TOF RPC wall in Au+Au beam at 1.25 A-GeV, *JINST* 8 (2013) P01004.
- [8] W.J. Llope et al., Multigap RPCs in the STAR experiment at RHIC, *Nucl. Instr. Methods A* 661 (2012) S110.
- [9] A. Akindinov et al., First commissioning results of ALICE-TOF SuperModules, *Indian J. Phys.* 85 (2011) 1155.

- [10] D. Bartos et al., Time Resolution of Radiation Hard Resistive Plate Chambers for CBM Experiment at FAIR, IEEE 978-1-4244-2715-4/08 (2008) N31–6.
- [11] M. Petrovici et al., High counting rate, two-dimensional position sensitive timing RPC, JINST 7 (2012) 11003.
- [12] D. Bartos et al., A method to adjust the impedance of the signal transmission line in a multi-strip multi-gap resistive plate counter, Rom. Journal of Physics 63 (2018) 901.
- [13] M. Petris et al., Towards a high granularity and high counting rate, differential readout timing MRPC, Nucl. Instr. Methods A 661 (2012) S129.
- [14] J. Wang et al., Development of high-rate MRPCs for high resolution time-of-flight systems, Nucl. Instr. Methods A 713 (2013) 40.
- [15] H. Yasuda, New insights into aging phenomena from plasma chemistry, Nucl. Instr. Methods A 515 (2003) 15.
- [16] S.Gramacho et al., A long run study of aging in glass timing RPCs with analysis of the deposited material, Nucl. Instr. Methods A 602 (2009) 775.
- [17] M. Petris et al., Performance of a two-dimensional position sensitive MRPC prototype with adjustable transmission line impedance, Nucl. Instr. Methods A 920 (2019) 100.
- [18] A. Senger, Design simulations of beam pipe and radiation studies for the CBM experiment, CBM-TN-18001 (2018).
- [19] IRASM irradiation facility, <https://www.nipne.ro/facilities/facilities/irasm.php>.
- [20] F.Anghinolfi et al., NINO:an ultra-fast and low-power front-end amplifier/discriminator ASIC designed forthe multigap resistive plate chamber, Nucl. Instr. Methods A 533 (2004) 183.
- [21] T.Nakajima et al., Preparation and electrical conductivity of florine-graphite fiber intercalation compound, Carbon 24 (1986) 343.
- [22] H.L.MacDonell, The use of Hydrogen Fluoride in the Development of Latent Fingerprints found on Glass Surfaces, Journal of Criminal Law and Criminology 51 (Article 10) 1960.
- [23] A.R.Frolov et al., Nucl. Instr. Methods A 307 (1991) 497.
- [24] Yi Wang, Update on Chinese low resistivity glass, RD51 Mini-Week, Dec. 7-9, 2015, CERN.
- [25] I. Burducea et al., A new ion beam facility based on a 3 MV TandetronTM at IFIN-HH, Romania, Nucl. Instr. Methods B 12-19 (2015) 12.
- [26] M.Mayer, SIMNRA User's Guide, Technical Report IPP 9/133, MPI fur Plasmaphysik, Garching, Germany [https://www2.ipp.mpg.de/ mam/](https://www2.ipp.mpg.de/mam/) (1977) 12.
- [27] M.Nastasi et al., SIMNRA User's Guide, Ion Beam Analysis: Fundamentals and Applications Taylor&Francis Group, LLC (2015) 12.
- [28] C.Jeynes et al., Thin film depth profiling by ion beam analysis, Analyst 141 (2016) 5944.
- [29] G. Binning et al., Atomic Force Microscope, Phys.Rev.Lett. 56 (1986) 930.
- [30] C. Möler et al., Tapping-Mode Atomic Force Microscopy Produces Faithful High-Resolution Images of Protein Surfaces, Biophys. J. 77 (1999) 1150.
- [31] I. Burducea et al., Characterisation of Indium Nitride and Zinc Oxide Thin Films by AFM and RBS, Romanian Journal of Physics 3-4 (2013) 345.